

Analysis of thermal strains and stresses in heated fibre metal laminates

Anisimov, A. G.; Müller, B.; Sinke, J.; Groves, R. M.

DOI

[10.1111/str.12260](https://doi.org/10.1111/str.12260)

Publication date

2018

Document Version

Final published version

Published in

Strain: an international journal for experimental mechanics

Citation (APA)

Anisimov, A. G., Müller, B., Sinke, J., & Groves, R. M. (2018). Analysis of thermal strains and stresses in heated fibre metal laminates. *Strain: an international journal for experimental mechanics*, 54(2), Article e12260. <https://doi.org/10.1111/str.12260>

Important note

To cite this publication, please use the final published version (if applicable). Please check the document version above.

Copyright

Other than for strictly personal use, it is not permitted to download, forward or distribute the text or part of it, without the consent of the author(s) and/or copyright holder(s), unless the work is under an open content license such as Creative Commons.

Takedown policy

Please contact us and provide details if you believe this document breaches copyrights. We will remove access to the work immediately and investigate your claim.

Green Open Access added to TU Delft Institutional Repository

'You share, we take care!' - Taverne project

<https://www.openaccess.nl/en/you-share-we-take-care>

Otherwise as indicated in the copyright section: the publisher is the copyright holder of this work and the author uses the Dutch legislation to make this work public.

Analysis of thermal strains and stresses in heated fibre metal laminates

A. G. Anisimov¹  | B. Müller²  | J. Sinke² | R. M. Groves¹ 

¹ Aerospace Non-Destructive Testing Laboratory, Structural Integrity and Composites, Delft University of Technology, Kluyverweg 1, 2629 HS Delft, The Netherlands

² Structural Integrity and Composites, Delft University of Technology, Kluyverweg 1, 2629 HS Delft, The Netherlands

Correspondence

A. G. Anisimov, Aerospace Non-Destructive Testing Laboratory, Structural Integrity and Composites, Delft University of Technology, Kluyverweg 1, 2629 HS Delft, The Netherlands.
Email: A.G.Anisimov@tudelft.nl

B. Müller, Structural Integrity & Composites, Delft University of Technology, Kluyverweg 1, 2629 HS Delft, The Netherlands.
Email: bernhard.muller@gmx.com

Funding information

H2020 project EXTREME, Grant/Award Number: 636549; Fokker Aerostructures; Dutch Technology Foundation STW

Abstract

Current trends in aircraft design are to increase the economic efficiency by integrating different features in multifunctional materials. One strategy is to embed resistance heater elements between glass-fibre epoxy layers in (heated) fibre metal laminates and to use them as anti or de-icing devices in leading edges of wings. Heated glass fibre reinforced aluminium (GLARE) is an example of such a multifunctional material where heating functionality was added to the (certified) structural feature of GLARE. As heated fibre metal laminates are an innovative and rather new material, the possible (local) effects of embedded heating on the stress–strain state have not yet been investigated. This research couples experimental characterisation of heated GLARE surface behaviour and numerical modelling analysis to investigate the surface and the through-the-thickness strain–stress state and temperature distributions due to the embedded heating. For the experimental part, the surface strains and the temperatures of a developed specimen were measured in a slow heating regime (temperature increase from 22.7 to 39.4 °C within 120 s) using, respectively, a developed shearography instrument and thermocouples with an infrared camera. Then a numerical model of heated GLARE was developed and verified with experimental results. Further, the numerical model was used to predict strains, stresses, and temperatures during a temperature increase similar to that used for de-icing in a real operation (temperature increase from –25 to 86.7 °C within 4.8 s).

KEYWORDS

fibre metal laminate, finite element method, heated GLARE, shearography, strain measuring

1 | INTRODUCTION

Combining current trends towards electric aircraft^[1] and the well-known problem of icing of leading edges^[2,3] lead to integrating resistance heater elements in laminated materials such as fibre metal laminates (FMLs).^[4,5] These materials combine structural and heating functions and are developed for the de- and anti-icing of aircraft leading edges. During icing conditions, de-icing systems frequently switch on their heating device for several seconds. Hence, they allow the build-up of (thin) ice layers and frequently melt them away.^[2] Contrary to this, anti-icing systems constantly switch on their heating device and avoid any ice build-up.

The potential of FMLs such as glass fibre reinforced aluminium (GLARE) has been explored over several decades.^[6,7] GLARE is the acronym of glass fibre reinforced aluminium laminate. Previous studies showed that the laminated structure of GLARE makes it a preferable material to design damage-tolerant parts as it has a lower fatigue crack growth rate compared to monolithic aluminium,^[8] and compared to pure glass fibre laminates, GLARE has enhanced strength bearing capabilities, together with favourable impact and lightening resistance.^[6,9] Furthermore, embedding the glass fibre-epoxy prepreg layers between the aluminium layers leads to better ultraviolet (UV)- and moisture-resistance.^[6]

Heated GLARE is an example of a multi-functional material where heating functionality has been added to the (certified) structural feature of GLARE. Figure 1 shows the layup of a nonsymmetric heated GLARE 5–4/3–0.3 laminate. GLARE is composed of alternating layers of aluminium and unidirectional (UD) S-2 glass fibre-epoxy prepreg layers.^[10] The heater elements are embedded between two UD-glass fibre-epoxy (90/90) prepreg layers and are positioned closer to the side where the ice is expected to build up, with the aim of concentrating the heating power there.^[11,12]

GLARE itself is an anisotropic material, which is manufactured in the autoclave.^[13] The different thermal expansion coefficients of the materials and the elevated curing temperatures during manufacturing lead to thermal residual stresses at room temperature.^[14,15] In addition to these thermal residual stresses, cold forming of GLARE panels can cause mechanical residual stresses.^[6] Those accumulated residual stresses superimpose with mechanical and thermal service loads. Thermal loading (passive) of the whole aircraft happens during the ascent and descent of aircraft (once per flight). Embedding (copper) heater elements increases the complexity of the material further and (actively) exposes the leading edges to frequent local thermal loads during the de- or anti-icing measures.^[16]

As heated FMLs and heated GLARE are an innovative and rather new material, the possible (local) effects of the embedded heating on the stress–strain state during (local) heating have not yet been investigated. Hence, the main focus of this research is on the analysis of thermal strains and stresses in FMLs, which are caused by the local embedded heating. This paper supplements the previous conducted researches on FMLs and GLARE, which addressed the temperature dependent material characteristics,^[13] residual stresses,^[14,15] the temperature distribution,^[17] the long-term behaviour,^[18] and thermal fatigue effects^[19,20] of GLARE and FMLs.^[16,21,22] This research includes the experimental measuring of the surface strains caused by the embedded heating and numerical modelling of the stress–strain state and temperature distributions. For the experimental part, a GLARE specimen with the embedded heater element was manufactured and inspected. The surface strains and the specimen temperatures were measured in the slow heating regime when the heater element temperature increased from 22.7 to 39.4 °C within 120 s. The surface strains were measured with a developed multicomponent shearography (speckle shearing interferometry) instrument.^[23] Shearography was used as it is a full-field non-destructive inspection (NDI) technique with high sensitivity to in- and out-of-plane surface displacement gradients. The specimen temperatures were measured with thermocouples and an infrared camera. Further, a numerical model was developed and verified with experimentally measured surface strains and surface temperatures in the aforementioned slow heating regime. The stress–strain state and temperature distributions were numerically modelled and analysed in the slow heating regime and a real-life de-icing regime with the heater element temperature increase from –25 to 86.7 °C within 4.8 s.

The main aim of the numerical modelling was to assess and analyse through-the-thickness information on the temperature distributions and stress–strain state during the heating phase when the highest stresses are expected. These through-the-thickness assessments were of the main practical interest as they reveal information, which cannot be obtained with conventional NDI techniques. The modelling does not cover questions related to the embedded heating as the thermal analysis (with heat transfer optimisation) or the assessment of the cyclic use of the anti- or de-icing system resulting in cyclic fatigue. These stand-alone research questions are out of the scope of this paper. The experimental assessment of the thermal cycling was reported earlier.^[16,22] The value of this research is in the coupling of the

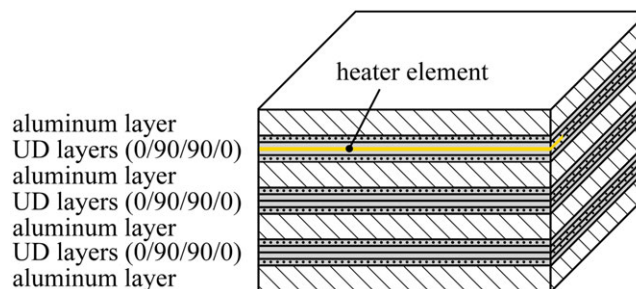


FIGURE 1 Heated glass fibre reinforced aluminium (GLARE) 5–4/3–0.3 layup

experimental results on the surface behaviour characterisation (strain, temperature) with the numerical analysis revealing the through-the-thickness information on the temperature distributions and stress–strain state during the embedded heating of GLARE.

2 | GLARE SPECIMEN DESIGN, MANUFACTURING, AND INSPECTION

For the experimental part of the research, a GLARE 5–4/3–0.3 specimen with embedded heater element was manufactured and inspected. The specimen was cured in an autoclave at a temperature of 120 °C and a pressure of 6 bar. The (heated) GLARE 5–4/3–0.3 laminate consisted of four 0.3 mm thick aluminium layers and three glass fibre-epoxy prepreg layers. Each glass fibre-epoxy prepreg layer (Figure 1) consisted of four 0.13 mm thick UD-glass fibre-epoxy prepreg layers with fibre orientations of (0/90/90/0).^[5,6] The total specimen thickness was 2.80 mm. A GLARE 5 layup was used due to its enhanced impact resistance compared to a GLARE 3 layup where each prepreg layer consists of two UD-glass fibre-epoxy prepreg layers. These two additional UD-glass fibre-epoxy prepreg layers in GLARE 5 increase the heat conduction coefficient due to their lower heat conduction coefficient compared to aluminium.^[13]

Figure 2(a) shows a fragment of the ultrasonic C-scan including the in-plane heater element position. A heater element on the right side of the scan was not used in this research. The plate thickness was 2.8 mm. The plate dimensions were chosen so that the part of the heater elements in the measured regions, that is, with a width of 2.5 mm and a length of 150 mm, had a distance from the edge of the plate of 200 mm. The area, which was later modelled numerically, is also shown in Figure 2(a).

Figure 2(b) shows the shape of the 0.13 mm thick copper heater element. In the measured region, the heater element width was 2.5 mm as it is used in the industry.^[5] The shape of the heater elements was deliberately simplified in order to get reliable experimental results on the material behaviour during the heating phase. The heater element width was increased to 10 mm to keep the temperature increase outside the measured region minimal and to avoid effects from the specimen edges. Hence, the (local) heating of the specimen was concentrated in the specimen centre. Preliminary temperature measurements during heating with the embedded heater elements confirmed this. Figure 2(b) also depicts the position of the embedded thermocouple before the lamination. The thermocouple was embedded at $y = 0$ mm and a distance of $\Delta x = 5$ mm next to the heater element. The heater element and the thermocouple were embedded between the second and the third UD-glass fibre-epoxy prepreg layers and aligned with the 90° fibres (cf. Figure 1). After manufacturing, the specimen was inspected using an ultrasonic C-scan instrument and the initial surface shape was measured using the shape measurement algorithms of a 3D digital image correlation (DIC) instrument.^[24] Figure 2(a) depicts the C-scan results. No delaminations were detected in the vicinity of the heater element. Figure 3 shows the

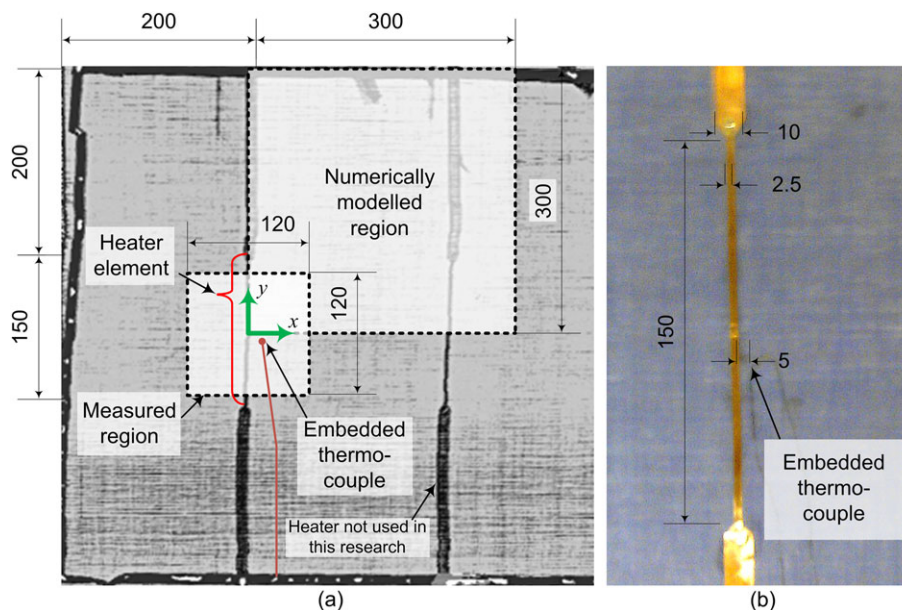


FIGURE 2 The manufactured specimen design: (a) a fragment of the ultrasonic C-scan of the specimen with the heater element, (b) photograph of the embedded heater element and the thermocouple during the manufacturing (units in mm)

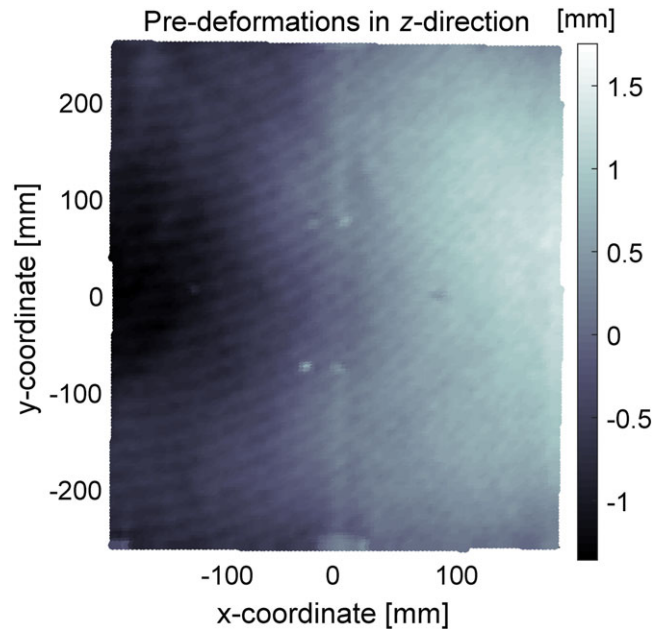


FIGURE 3 Three-dimensional digital image correlation measurements: pre-deformation of the manufactured specimen in the region with the embedded heater element and adjacent area including the region measured with shearography and some outer areas

initial specimen geometry measured with the 3D DIC technique at room temperature and covers the region measured with shearography and some outer areas. A predeformation resulting from the manufacturing process, that is, the slightly nonsymmetric layup, could be identified. The predeformation defined as the specimen shape deviation from an expected flat surface was an unintended result of factors affecting the manufacturing and the influence of the embedded copper pieces, which made the layup nonsymmetric. The contributed factors affecting the manufacturing process included nonflatness of the base plate and predeformations of the aluminium layers. A visible ring-pattern in 2D plot is an unintended result of the spatial aliasing, which affected the 3D DIC measurements due to not high enough spatial resolution of the DIC instrument in respect to the physical size of the painted speckle pattern.^[25,26] The painted speckle size was optimised for closer measurements.

3 | MEASURING SURFACE STRAIN COMPONENTS AND TEMPERATURE

In this research, a developed multicomponent shearography instrument was used to measure the surface strain components of the manufactured specimen in the slow heating regime (temperature increase from 22.7 to 39.4 °C within 120 s). The specimen temperatures were measured with thermocouples and an infrared camera. The experimental results were later used for verification of the developed numerical model.

3.1 | Shearography—Experimental set-up

Shearography provides a full-field direct measurement of the surface displacement gradients including the in- and out-of-plane surface components. The measurement principle is based on a correlation analysis of interferometric speckle patterns captured before and after the surface deformation. Shearography theory and the principle of its operation as an NDI technique are well described in literature.^[23,27–29] Figure 4 shows the developed multicomponent shearography instrument with its multiple viewing and single illumination configuration.^[30–32] A multicomponent configuration with three viewing directions was used to isolate the surface strain components ($\partial u/\partial x$, $\partial v/\partial x$, and $\partial w/\partial x$) for the shear in x -direction and ($\partial u/\partial y$, $\partial v/\partial y$, and $\partial w/\partial y$) for the shear in the y -direction, where u , v , and w are surface displacements along x , y , and z , respectively.^[33,34]

A detailed description of the developed shearography instrument was previously reported.^[30–32] Technical parameters of the developed instrument and a brief description of the measuring procedure are given below for a possible comparison with other shearography instruments. Three spatially distributed shearing cameras and the laser

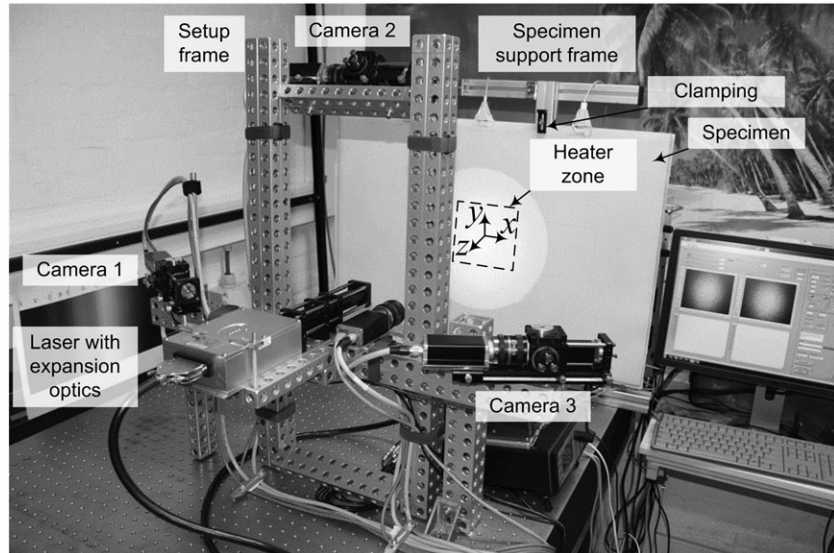


FIGURE 4 Experimental set-up with the multicomponent shearography instrument

with expansion optics were placed in a “T”-configuration using an Alufix modular fixture system (Witte Barskamp KG, Bleckede, Germany). Torus 532 laser (optical power of 500 mW and wavelength of 532 nm by LASER QUANTUM, Stockport, England) was used. The cameras were calibrated in pairs as stereovision systems to identify their locations and to provide imaging lenses distortion correction.^[35–37] Shearing cameras consisted of Pilot piA2400 cameras (Basler AG, Ahrensburg, Germany) with Linos MeVis-C 1.6/25 imaging lenses (Qioptiq Photonics GmbH, Gottingen, Germany) and shearing devices based on Michelson interferometers.

Image shearing and phase shifting were performed by controlling one of the mirrors in each shearing camera using a three coordinate piezo-electric actuator PSH 4z (Piezosystem Jena, Jena, Germany). A simple three-step phase shifting method was used due to the minimal number of piezo movements and images, which were taken.^[28] The shearing distances in the x - and y -directions were calibrated for the region of interest (ROI) for each camera with mean values close to 1 mm.^[32] In Figure 4, the ROI used in this study is marked with dashed lines with dimensions of 120×120 mm. The heater element was in the ROI centre. The specimen was positioned in front of the shearography instrument at a working distance of 500 mm and clamped to a support frame in its four corners.

3.2 | Thermal loading and temperature measurement in the slow heating regime

Figure 5(a) shows the positions where the temperatures were measured using two surface mounted thermocouples (TC) and one embedded TC and an infrared (IR) camera. Figure 5(b) shows the temperatures at these positions during resistance heating in the slow heating regime. Thermocouples TC1 and TC2 were applied at the specimen surface whereas TC3 was embedded between the second and third UD-glass fibre-epoxy prepreg layers adjacent to the heater element, as shown in Figure 2. TC1 was applied at the heater element centre at $x = y = 0$ mm. TC2 and TC3 were positioned at $x = 5$ and $y = 0$ mm. Furthermore, Figure 5(a) displays the 2×2 mm area where the temperature was measured by FLIR A65 IR camera. Averaging across the IR zone was performed later to minimise the local variation of the surface emissivity caused by the thermocouple, which was attached to the surface. Furthermore, the overall spatial temperature distribution across the ROI was measured with the IR camera. The ambient specimen temperature was 22.7 ± 0.5 °C.

The thermal loading of the specimen was performed by resistance heating of the heater element in the slow heating regime where the temperature of the heater element increased from 22.7 to 39.4 °C within 120 s (Figure 5(b)). The heater element was subjected to constant electrical power of 30 W for 120 s. The slow heating regime was introduced to meet the maximum arising strain rate with the performance of the shearography instrument. The shearography instrument used in this research was limited to a data acquisition time of 4 s because of the piezo-electric actuators settling time and the frame rate of the cameras.^[30] So 30 sets of phase-shifted interferograms were recorded during the thermal loading. These sets were processed as sequential load steps.^[28]

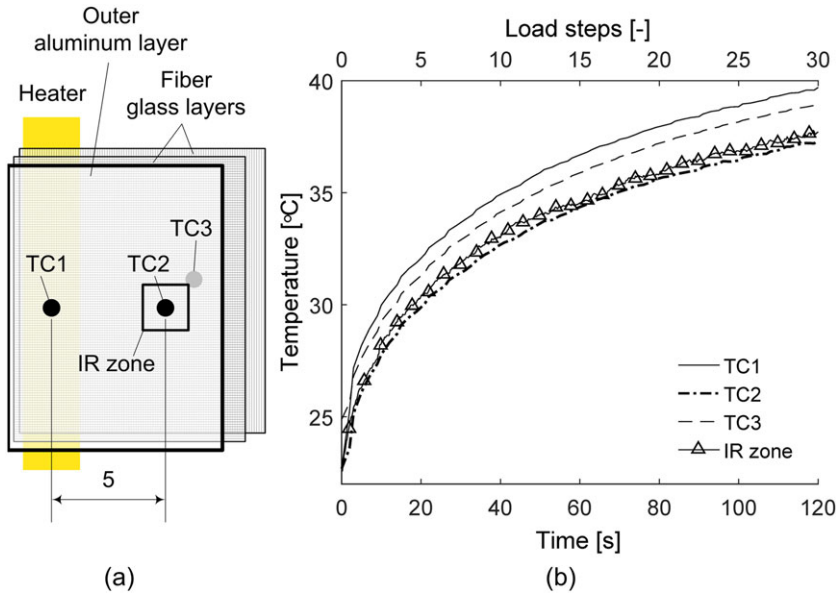


FIGURE 5 Thermal loading in the slow heating regime: (a) location of thermocouples and infrared (IR) camera measuring zone and (b) measured temperatures due to the resistance heating of the heater element

3.3 | Surface strain distributions in the slow heating regime

Figures 6(a) to 6(f) show the measured surface strain components $\partial v/\partial x$, $\partial w/\partial x$, $\partial u/\partial y$, $\partial w/\partial y$, $\partial u/\partial x$, and $\partial v/\partial y$ in the ROI of the shearography instrument at the end of the thermal loading in the slow heating regime. Two normal strains, ε_{xx} and ε_{yy} , in the x - and y -directions and the shear strain ε_{xy} are obtained from

$$\varepsilon_{xx} = \frac{\partial u}{\partial x}, \quad \varepsilon_{yy} = \frac{\partial v}{\partial y}, \quad \varepsilon_{xy} = \frac{1}{2} \left(\frac{\partial u}{\partial y} + \frac{\partial v}{\partial x} \right). \quad (1)$$

Figure 6(g) shows the associated graph of the calculated shear strain component ε_{xy} . Figures 6(e) to 6(g) with the surface strain components ε_{xx} , ε_{yy} , and ε_{xy} were enlarged as they were used further for the numerical model verification.

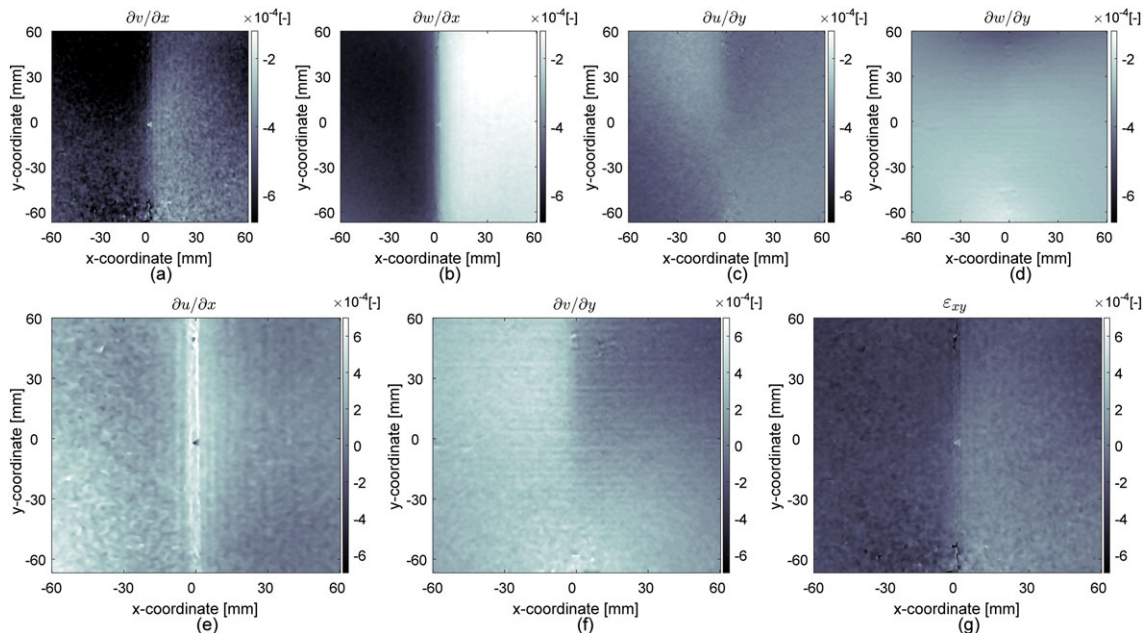


FIGURE 6 Surface strain components for the heater element: (a–g) strain maps across the surface in the region of interest 120×120 mm ($1,278 \times 1,347$ pixels) at $t = 120$ s

Figure 6(e) shows positive values of the surface strain component $\partial u/\partial x$, which means that the material expanded in the x -direction. Locally high values of $\partial u/\partial x$ up to $7 \cdot 10^{-4}$ were recorded in the vicinity of the heater element, that is, $|x| \leq 1.25$ mm. The strain levels in the outer regions were lower. The strain distribution of $\partial u/\partial x$ was almost symmetric in respect to the heater element and varied slightly along the heater element. Figure 6(f) shows lower magnitudes for the surface strain component $\partial v/\partial y$ and no peaks in the vicinity of the heater element. However, in the upper right quadrant, negative values of $\partial v/\partial y$ were recorded, which indicated compressive strains.

4 | NUMERICAL ANALYSES

4.1 | Numerical model

A three-dimensional numerical model of the GLARE specimen with embedded heater element was developed for the analysis of the stress–strain state and temperature distributions. Firstly, the model was used to predict the stress–strain state and temperature distributions in the slow heating regime. The modelling results were compared with the experimental ones. The through-the-thickness assessment of the stress–strain state and temperature distributions were done supplementary to the two-dimensional strain and temperature mapping of the measurements. Secondly, the model was used to predict stress–strain state and temperature distributions for a heating curve on the basis of expected de-icing conditions.^[22] This regime was defined as the de-icing regime. The transient coupled thermal analyses were conducted with the finite element (FE) code Abaqus (Dassault Systemes, Velizy-Villacoublay, France).

Figure 2(a) shows the modelled area of 300×300 mm with dashed lines including the coordinate system with the origin at the centre of the heater element ($x = y = 0$ mm) at the top surface ($z = 0$ mm). A double symmetric model was used due to the symmetry about the x - and y -axes of the dimensions, the material (layup and position of the heater element), and the (thermal) loading conditions, that is, temperatures. Thus, the required computational resources were reduced to a quarter. The plate was modelled as perfectly flat as the relatively complex, but relatively small predeformations were difficult to include exactly in the model. Furthermore, their exact distribution through the thickness in the vicinity of the heater element(s), that is, the predeformations in each laminate layer including the embedded heater element, could not be determined using the applied surface measuring techniques.

The complex laminate material was accounted for by modelling the GLARE 5–4/3–0.3 plate with the embedded heater element as one part, which was separated in sections with assigned material properties according to Figure 1. Using sections to assign different material properties leads to a perfect bond and heat conduction between the (different) modelled material layers. The material properties were taken from Hagenbeek^[13] and Kundig.^[38] They take into account the temperature dependence of the thermal expansion coefficients, the heat capacity, and the heat conduction coefficients of the FM94 glass-fibre epoxy at moderate temperatures. The orthotropic material behaviour of the FM94 UD glass-fibre epoxy layers was modelled through different material parameters in and perpendicular to the fibre direction of the layers. Thereby, the material properties of the fibres and the epoxy were averaged in each direction in respect to their volume fraction.

The element size in-plane varied through the model. In the vicinity of the heater element, the temperature gradients in the x -direction were highest. Therefore, a finer mesh with element dimensions of 0.16 mm was used in the region $0 < x < 2.5$ mm. With increasing distance from the heater element, the element dimensions were increased in three steps to 5 mm. In the z -direction, the element size was the same across the model. Each UD-layer and the copper mesh were discretised with two elements across the thickness. The aluminium layers were discretised with three elements, which lead to 0.07 to 0.1 mm thick elements.

Statically determined mechanical boundary conditions were used. For all elements along the x -axis, the displacements in the y -direction and the rotations about the x - and z -axes were locked, and for all elements along the y -axis, the displacements in the x -direction and the rotations about the y - and z -axes were locked. Furthermore, the displacements in the z -direction were locked at $x = y = 300$ mm. The choice of the modelled area of 300×300 mm, which is larger than the ROI of the shearography instrument (as shown in Figure 2(a)), was made to model the boundary conditions in the x - and y -directions properly. As the elements at the outer areas of the modelled area were relatively large (up to 5 mm), the additional modelled area added accuracy to the modelling results without severely adding calculation time.

The thermal loading of the model was performed in three steps. Table 1 shows these steps. Steps 1 and 2 were used to simulate the manufacturing (curing) process of the GLARE laminate in the autoclave to account for thermal residual stresses. Thus, in the first step, the (initial) conditions, which are found in the autoclave during curing, were defined, that

TABLE 1 Load steps in the numerical model

Step	Name	Description
1	Initial	Conditions during curing (whole specimen): 120 °C and 6 bar
2	Residual stresses	Pressure reduction from 6 to 0 bar
	a. Slow heating regime	Temperature decrease (whole specimen) from 120 to 22.7 °C within one time step
	b. De-icing regime	Temperature decrease (whole specimen) from 120 to −25 °C within one time step
3	Heating	
	a. Slow heating regime	Temperature increase of the heater element: 22.7 to 39.4 °C within 120 s
	b. De-icing regime	Temperature increase of the heater element: −25 to 86.7 °C within 4.8 s

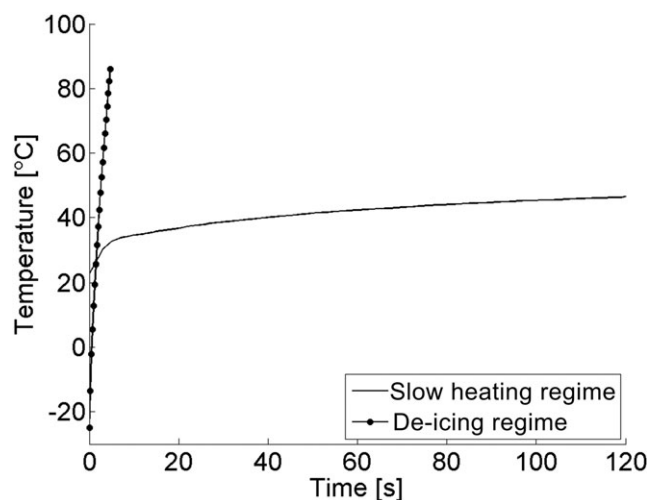
is, a temperature of 120 °C and a pressure of 6 bar. In the second step, the atmospheric pressure was decreased from 6 to 0 bar. To account for the two different heating regimes, the temperatures were linearly decreased to 22.7 °C (the slow heating regime, Step 2a) and −25 °C (de-icing regime, Step 2b), respectively. According to Abouhamzeh,^[39] this linear elastic approach gives a reasonable estimation of the thermal residual stresses.

The third step simulates the local thermal loading by the embedded heater element. Figure 7 shows the two different temperature profiles, which were used for the third step. Firstly, the measured temperature profile in the slow heating regime (Step 3a) was used to verify the numerical results with the measured temperatures and surface strains (cf. Section 3). Secondly, a temperature profile similar to the heating phase during de-icing conditions (Step 3b) was used to predict the temperatures, strains, and stresses.

The numerical modelling for Step 3a was performed based on the measured temperature profile and not the applied electrical power (cf. Section 3.2). The measured temperature profile was considered to be more reliable input data than the applied power as the embedded heater element had a complex shape (Figure 2(a)) with external wiring. So the actual amount of the electrical power applied directly to the 2.5 mm width part of the embedded heater element was unknown.

The thermal loading conditions from the slow heating regime (Step 3a) were simulated by extrapolating the measured (surface) temperatures in Figure 5 to predict the temperatures of the heater element in the slow heating regime (see Figure 7). Those temperatures were then used as a thermal boundary (loading) condition and defined the temperature increase of the heater element. Further thermal boundary conditions were considered by defining a surface film condition for the convection and a surface radiation for the radiation. The parameters were chosen according to the vertically positioned and matt white sprayed plate (cf. Figure 4).

The thermal loading conditions of the de-icing regime (Step 3b) were applied to simulate possible temperature and stress distributions at de-icing conditions (see the de-icing regime curve in Figure 7). The heating curve of the de-icing regime was based on the measured temperatures during the thermal cycling experiments with heated GLARE conducted by Müller.^[22] In order to model the scenario where the largest residual stresses were expected and icing can occur, the initial specimen and ambient temperatures were decreased to −25 °C, that is, the measured curve was shifted so that the

**FIGURE 7** Input heater element temperatures in the numerical model for the slow heating and the de-icing regimes

minimal value of the heating curve was $-25\text{ }^{\circ}\text{C}$. This shifting of the curve was done as icing was expected to happen at temperatures between -25 and $+10\text{ }^{\circ}\text{C}$, and the residual stresses due to manufacturing tend to increase with the temperature difference from the actual and the curing temperatures during manufacturing.^[12,16]

In summary, this means that for the simulation of the de-icing regime, the model temperature was decreased to $-25\text{ }^{\circ}\text{C}$ (Step 2b) and then locally heated with the embedded heater element from -25 to $+86.7\text{ }^{\circ}\text{C}$ within 4.8 s (Step 3b). The modelled ambient temperature was $-25\text{ }^{\circ}\text{C}$. The calculation was stopped after 4.8 s as this research focused on examining the heating phase where highest stresses were expected. Due to the local heating during the heating phase, the (local) temperature differences in regions with the highest number of different materials (in the vicinity of the heater elements) were expected to be higher compared to the expected temperature differences during the cooling phase (icing) where the cooling was expected to happen more globally across the whole (outer) surfaces.

4.2 | Numerical analyses of the slow heating regime

The numerical model was verified by comparing the measured and numerically predicted (surface) temperatures and strains of the heater element. Figure 8 shows the temperature differences of the measured and the numerically predicted temperatures in the vicinity of the heater element. Although, the temperature gradients in the vicinity of the heater element were high, their shapes and magnitudes matched. The maximum surface temperature differences between the measured and numerical results were $0.25\text{ }^{\circ}\text{C}$ above the heater element (TC1-TC1 FEM) and $0.45\text{ }^{\circ}\text{C}$ at a distance of 5 mm from the heater element (TC2-TC2 FEM) during the whole heating phase. Similarly, the temperatures measured in the laminate using the embedded thermocouple TC3 and numerical results TC3 FEM differ by less than $1\text{ }^{\circ}\text{C}$ after the first seconds. During the first few seconds, the measured temperatures using the embedded thermocouple TC3 differed not only from the numerically predicted ones about $-22\text{ }^{\circ}\text{C}$ but also from the (measured) initial temperatures of the thermocouples TC1 and TC2 (see Figure 5(b)). Thus, the slightly higher temperature differences in the first few seconds were accepted as they resulted from the slightly higher temperatures inside the specimen compared to its surface temperatures ($\pm 0.5\text{ }^{\circ}\text{C}$).

Figure 9 shows the surface temperatures measured using the IR camera and the numerically predicted surface temperatures at the end of test at 120 s in the vicinity of the heater element. The graphs at the bottom and at the very right depict the numerically predicted temperature distributions through the thickness. The magnitudes and the shape of the temperature distributions match as the maximum (surface) temperature differences were less than $1.3\text{ }^{\circ}\text{C}$, that is, less than 3.3%. The temperature gradients above the heater element were the highest and constantly decreased with increasing distances from the heater element. The surface temperature locally increased from a room temperature of $22.7\text{ }^{\circ}\text{C}$ to a maximum temperature of $39.35\text{ }^{\circ}\text{C}$.

The measured (reference) and the numerically predicted (FEM) surface strain components ϵ_{xx} and ϵ_{yy} along the x -axis were compared in Figure 10(a). The trends agreed and the magnitudes of both surface strain components were comparable. The numerical model predicted a continuous decrease of the surface strain component ϵ_{xx} along the x -coordinate with a maximum value of $3.8 \cdot 10^{-4}$ at $x = 0\text{ mm}$ (above the heater element). The measured strain component at the same position was $3.3 \cdot 10^{-4}$. The absolute differences between the measured and numerical results varied due to the waviness

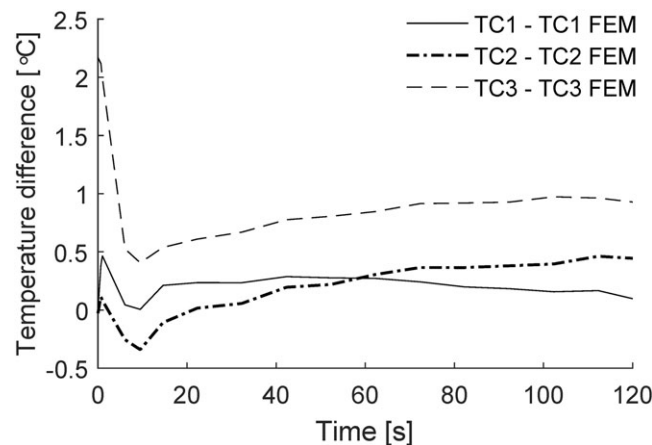


FIGURE 8 Temperature differences of the measured (thermocouples) and the numerically predicted temperatures at the positions indicated in Figure 5(a)

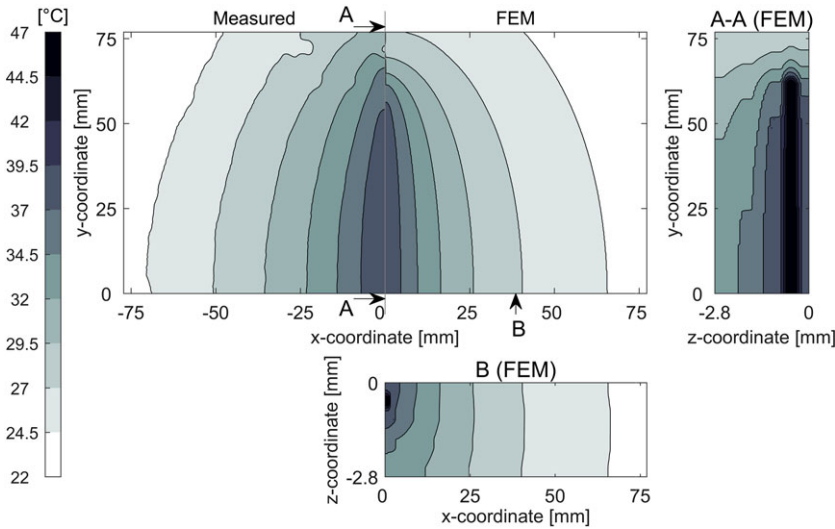


FIGURE 9 Surface temperatures of the specimen after 120 s in the vicinity of the heater element in the x-y-plane at z = 0 mm of the infrared (left) and the numerical model (right). The intersections A-A and B depict the temperatures at the y-z-plane at x = 0 mm and the x-z-plane at y = 0 mm. The z-direction was scaled with the factor 10

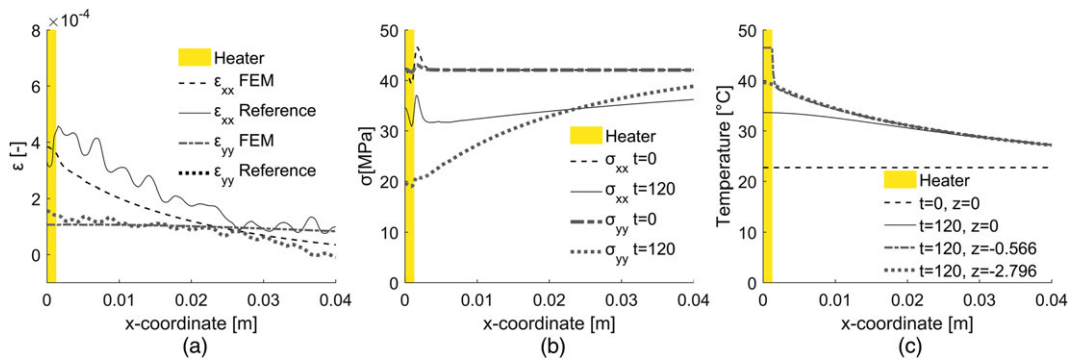


FIGURE 10 Comparison of the (a) measured and the numerically predicted surface strain components, numerical prediction of the (b) surface stresses, and (c) temperatures at the three different z-coordinates before (t = 0 s) and after (t = 120 s) the heating phase according to the slow heating regime at y = 0 mm

of the measured results locally of about $0.8 \cdot 10^{-4}$. The measured and numerically predicted strain components ϵ_{yy} agreed. The maximum differences were $0.9 \cdot 10^{-4}$. The position of the heater element was highlighted with a yellow bar in Figures 10, 11, 13, and 14.

Figures 10(b) and 10(c) present the surface stresses and temperatures at y = 0 mm along the x-coordinate before (t = 0 s) and after (t = 120 s) the (local) thermal loading by the heater element. The residual surface stresses due to manufacturing in the autoclave were predicted to be almost constant with a magnitude of 42.1 MPa and were

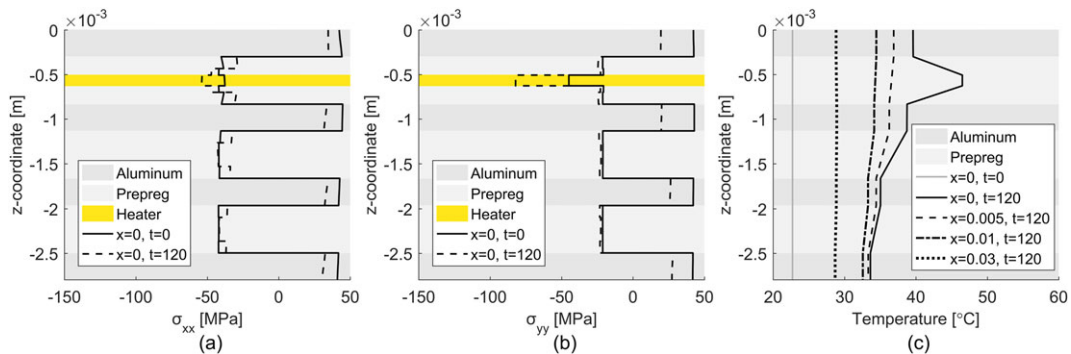


FIGURE 11 Numerically predicted stresses (a) σ_{xx} , (b) σ_{yy} at x = y = 0 mm, and (c) temperature distributions through the thickness before (t = 0 s) and after (t = 120 s) the heating phase according to the slow heating regime

comparable with values (30 MPa) found in the literature.^[14] Slightly higher thermal residual stresses were found due to using a GLARE 5 layup, which included more UD layers than the layup which Hofslagare used.^[14] However, stress peaks at the position of the embedded copper mesh were predicted ($-4.6/+2.8$ MPa).

Furthermore, Figure 10(b) shows that the almost constant (residual) stress distributions changed, and after 120 s, the stresses decreased nonlinearly towards the heater element with elevated temperatures. The different reductions after 120 s of the stresses σ_{xx} and σ_{yy} resulted from the different temperature distributions in the x - and y -directions when starting from $x = y = 0$ mm. The temperature in the x -direction decreased significantly with increasing distance from the heater element (see Figure 9). Contrary to this, the temperatures remained about constant above the heater element for increasing y -values. Thus, the temperature has elevated values along a larger distance in the y -direction, which leads to the more significant local stress reduction when heated locally using the embedded copper element.

Figure 10(c) shows the corresponding surface temperatures at $z = 0$ mm. Furthermore, it depicts the temperature distributions along the x -coordinate in the centre plane of the heater element ($z = -0.57$ mm) and at the opposite surface ($z = -2.80$ mm). The numerical model predicted a local temperature increase at $x = 0$ mm from 22.7 to 39.6 °C at the top surface, to 46.5 °C at the heater element and to 33.6 °C at the opposite surface. The temperature dropped severely at the heater element edges ($x = 1.25$ mm, $z = -0.57 \pm 0.07$ mm).

Figures 11(a) and 11(b) show the numerically predicted residual stresses ($t = 0$ s) and the stresses after the local thermal loading ($t = 120$ s) through the thickness at ($x = y = 0$ mm). The model predicted tension stresses in the aluminium layers and compressive stresses in the glass-fibre layers. The compressive (residual) stresses of the copper element changed most due to the (local) thermal loading. Different colours indicate the different material layers. The position of the heater element was between $-0.51 \geq z \geq -0.63$ mm.

Figure 11(c) shows the temperature distributions before and after the (local) thermal loading by the heater element, through the thickness at different distances from the heater element. The numerical model predicted that the local temperature peaks at the heater element ($x = 0$ mm) changed to a more homogeneous temperature distribution at distances of 5 mm from the x -axis. The temperature distributions for distances larger than 30 mm from the x -axis were predicted as constant through the thickness. Furthermore, the model predicted a slight temperature difference in the thickness direction of the aluminium layers but large temperature changes through the thickness in the glass fibre-epoxy layers. This almost stepwise temperature change resulted from the higher thermal conduction coefficient of the aluminium layers compared to the glass fibre-epoxy layers.

4.3 | Numerical analyses of the de-icing regime

Figure 12 shows the numerically predicted temperature increase at the top surface ($z = 0$ mm) and in the heater element centre plane ($z = -0.57$ mm) due to the local thermal loading in the de-icing regime (see Figure 7). The graphs show the temperatures above ($x = 0$ mm) and at several distances ($x = 2.5, 5, 10, 30$ mm) from the heater element centre during the heating phase, that is, from 0 to 4.8 s.

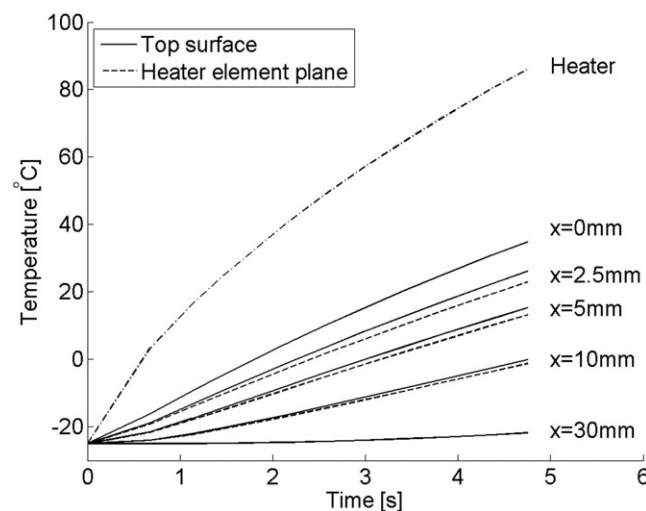


FIGURE 12 Predicted temperatures during the de-icing conditions of the heater (element) and at several positions at the top surface ($z = 0$ mm) and in the heater element plane ($z = -0.57$ mm) at $y = 0$ mm

Furthermore, Figure 12 visualises the rather local temperature increase due to heating with the heater element. The temperature of the heater element increased from -25 to 86.7 °C, and the surface temperatures above the heater element increased to 34.9 °C and at distances of 2.5 mm from the heater element to 26.1 °C at $z = 0$ mm and 23.0 °C at $z = -0.57$ mm. Furthermore, the differences between the top surface temperatures and the temperatures inside the material with equal x -coordinates decreased from 51.8 °C at the heater element ($x = 0$ mm) to almost 0 °C at distances of $x > 30$ mm.

Similarly to Figures 10 and 11, Figures 13 and 14 show the surface strains, stresses, temperatures and the stresses, temperatures through the thickness, respectively. Figure 13(a) visualises that the magnitudes of the surface strain components ϵ_{xx} and ϵ_{yy} increased with the higher temperatures of the de-icing regime in comparison with Figure 10(a) to maximum values of $16.7 \cdot 10^{-4}$ and $1.9 \cdot 10^{-4}$, respectively.

Figure 13(b) shows that the residual stresses ($t = 0$ s) at -25 °C were predicted to be 57.9 MPa with local peaks above the heater element of $\sigma_{xx}^{peak} = 62.6$ and $\sigma_{yy}^{peak} = 59.5$ MPa. The stress component σ_{xx} at the surface decreased due to the local heating to 52.0 MPa and showed a local minimum above the heater element of a similar magnitude as the residual stresses. After the heating phase ($t = 4.8$ s), the stress component σ_{yy} at the surface above the heater element locally decreased to -24.1 MPa and increased to 63.4 MPa at distances of $x = 40$ mm.

Figures 13(c) and 14(c) indicate the local temperature increase due to the local heating and show a considerable temperature drop at the edges of the heater element in the x - and z -directions. The numerical model predicted a temperature increase from -25 to -7.6 and 34.87 °C at $z = -2.80$ and $z = 0$ mm with a temperature peak of 86.7 °C at the heater element ($z = -0.57$ mm) after heating (cf. Figure 12).

Figures 14(a) and 14(b) show tensile residual stresses in the aluminium layers and compressive residual stresses in the glass fibre-epoxy layers at a temperature of -25 °C at $x = y = 0$ mm. The residual stresses ($t = 0$ s) in the aluminium showed values between 56.8 and 63.5 MPa in the bottom and top aluminium layers. The residual stresses in the glass fibre-epoxy layers were between -10.5 and -76.7 MPa. Compressive residual stresses between -49.9 and -62.4 MPa were predicted for the copper heater element.

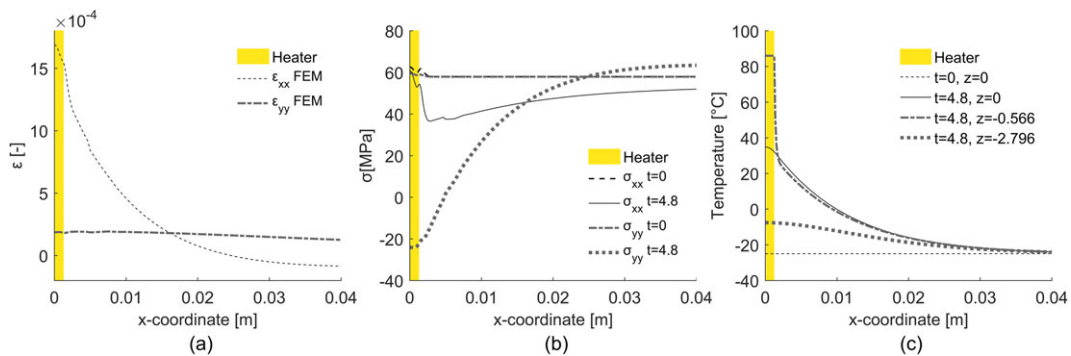


FIGURE 13 Prediction of the (a) surface strains, (b) surface stresses, and (c) temperatures at the three different z -coordinates along the x -axis before ($t = 0$ s) and after ($t = 4.8$ s) the heating phase according to the de-icing conditions

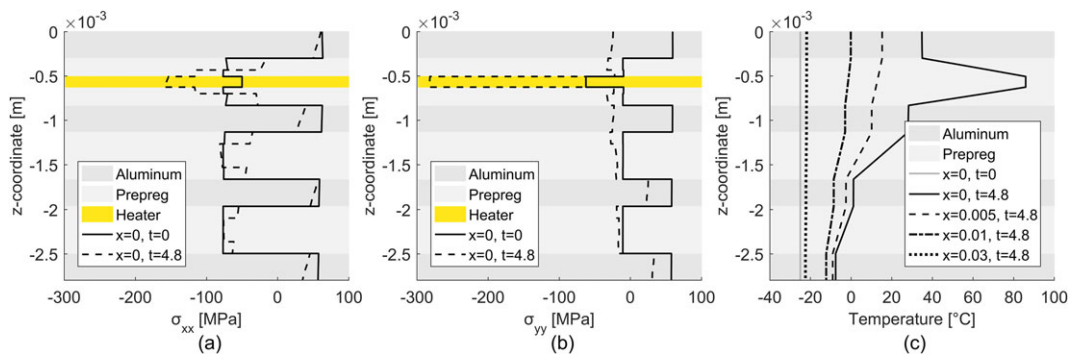


FIGURE 14 Numerically predicted stresses (a) σ_{xx} , (b) σ_{yy} at $x = y = 0$ mm, and (c) temperature distributions through the thickness before ($t = 0$ s) and after ($t = 4.8$ s) the heating phase according to the de-icing conditions

At the end of the heating phase ($t = 4.8$ s), the residual stresses σ_{xx} locally decreased in the vicinity of the heater element. The minimum value of -159.4 MPa was found at the heater element. The stress component σ_{yy} decreased even further to $\sigma_{yy} = -282.6$ MPa locally at the heater element. Hence, the predicted stresses in the heater elements reached magnitudes where the copper is expected to yield. Furthermore, the local heating decreased the magnitudes of the stress component across the whole thickness.

5 | DISCUSSION

The surface strain components of the developed specimen measured in the slow heating regime showed that some zones were compressed (negative values of the strain components), although the material was expected to expand (positive values of the strain components). Those zones were, for example, the zones at the edges of the ROI of the strain component $\partial u/\partial x$ in Figure 6(e) and the upper-right corner of the strain component $\partial v/\partial y$ in Figure 6(f). These zones with compressive strains were most probably a result of the predeformations introduced during the manufacturing process. Figure 3 shows such predeformations with varying values of the z -coordinate at the surface, for example, along the x -direction in the vicinity of the heater element ($|x| \leq 50$ mm). Those predeformations are expected to influence the deformations caused by the (local) thermal loading and lead to such compressed zones.

The waviness of the measured results is revealed in Figure 10(a), and it is also visible as fringe patterns in Figure 6 (e.g., vertical and horizontal patterns in Figures 6(e) and 6(f), respectively). This waviness, which may be a result of the layout, is not yet fully interpreted by the authors; therefore, the detailed explanation is out of the scope of this paper.

The slow heating regime was introduced based on the temporal performance of the shearography set-up (Figure 4). In order to measure the surface strains of heated GLARE in the de-icing regime (Figure 7), a higher frame rate of the cameras together with high-speed shearing and phase shifting devices are required. The comparison of the measured surface strains and temperatures with the numerically predicted ones showed a reasonable agreement in the slow heating regime. Hence, the numerical analyses were used to predict the (local) temperatures, strains, and stresses at the temperatures, which were expected during de-icing measures. Although the model was sophisticated, it did not include melting of the ice nor temperature changes due to forced convection including water droplets, which eventually appear during the de-icing of leading edges. For such simulations, different models and algorithms including fluid dynamics may be appropriate. The verifications of those models tend to be complex and connected with uncertainties. However, the temperature and stress distributions in the specimen of the current model can be used as an estimation of the material state for further research in the field of heated GLARE because they show during a certain computational time the impact of one out of many possible anti-icing temperature distributions, which depend, for example, on the aircraft velocity, humidity, internal, and external temperatures. Furthermore, the precision of the numerical model was increased by taking the temperature-dependent, orthotropic material behaviour and the thermal residual stresses into account.

The stress peaks, which were caused by localised temperature increases and the different thermal expansion coefficients, are expected to have effects on the fatigue life of heated FMLs. Two different effects were expected. The first was that the elevated temperatures might affect the material properties of the individual materials (glass fibre-epoxy, aluminium, and copper) and their interfaces. Aging of the epoxy is one of the most likely effects at elevated temperature ranges.^[21] The second expected effect is that the local temperature increases and the different thermal expansion coefficients lead to local (mechanical) stress concentrations, especially at the heater elements. These locally high stresses might be equivalent to a mechanical fatigue loading in the vicinity of the heater elements in heated FMLs. Thus, possible changes of the material characteristics are expected in the vicinity of the heater elements due to elevated temperatures and mechanical fatigue loading conditions during the locally fast temperature changes. The experimental assessment of the thermal cycling was reported earlier.^[16,22] A complete (numerical and experimental) assessment of the thermal cycling is one of the directions of future research.

Different heater element shapes and heating rates cause different temperature distributions and consequently different (local) stress concentrations due to different material properties and temperatures. Thus, peak stresses can be reduced by slower temperature increase rates as the (local) temperature differences decrease with decreasing heating rate (cf. Figures 10 and 11 with 13 and 14). Consequently, the shape and dimension optimisation of the heater elements used in aircraft leading edges should be done in respect to both the minimal heating power to melt the ice and the minimal thermal stresses. However, the upper limit of the service temperature in heated GLARE laminates is limited by the epoxy and lies for standard GLARE about 80 °C (FM94) and for high static strength GLARE about 120 °C (FM906).^[13,40]

According to the design suggested in other work,^[5] several s-shaped heater elements are applied next to each other at distances of 2.5 to 5 mm. The heated regions of the neighbouring heater elements interfere and, consequently, heat the (surface of) leading edges more effectively and uniformly. Additionally, the relatively high heat conductivity of the aluminium layer (at the surface) facilitate a homogeneous heat distribution. The surface temperatures are expected to increase faster due to the interfering heating zones of the embedded heater elements. Furthermore, a more uniform temperature increase is expected to decrease thermal stress concentrations at the heater elements.

Different heater element materials could be less effective in terms of power consumption or heating, but the use of different heater materials might be beneficial in terms of thermal (residual) stresses, structural performance, and environmental resistance (e.g., corrosion). Alternatively, carbon heater meshes could be used. Carbon heater meshes could be used as structural elements and thus would possibly lead to weight savings. The use of aluminium heater elements would possibly decrease stress peaks, as at the beginning of the local heating phase, the differences of the thermal residual stresses due to the different thermal expansion coefficients would locally decrease. As the tensile stressed aluminium heater element would heat up first causing a local stress relief instead of a stress increase as shown in Figures 13 and 14. Furthermore, the use of aluminium heater elements would not cause any additional corrosion issues, which might be introduced by the combination of aluminium layers and copper or carbon heater elements in heated GLARE when affected by (salt) water during service life of aircraft.

One option, which would enable the positioning of the heater elements even further towards the outer surface of leading edges (where the maximum temperature is needed), is to use electrically nonconductive coatings for the heater elements. If such coatings could electrically isolate the (copper) heater elements and the (outer) aluminium layer and still would guarantee a good heat conduction, then the heater elements could be positioned directly on the outer aluminium layer without UD glass fibre-epoxy prepreg layers in between.

6 | CONCLUSION

The presented results show the ability of multicomponent shearography to quantitatively characterise the surface strains of heated FMLs. The measured in-plane surface strain components were used to verify the numerical model in the slow heating regime with the (local) temperature increase from 22.7 to 39.4 °C within 120 s.

The three-dimensional numerical model was verified in the slow heating regime and applied to predict temperatures, strains, and stresses through the thickness supplementary to the two-dimensional strain and temperature measurements. The temperatures during the whole heating phase matched. The maximum difference at the surface was 0.9 °C. The trends of the surface strains agreed, and their magnitudes were comparable. According to the numerical results, the thermal residual stresses were important to be taken into account for the prediction of the stress concentrations. These stress concentrations resulted from different thermal expansion coefficients and the localised thermal loading with the embedded copper heater elements, which introduced (high) local temperature differences.

Furthermore, the numerical analyses were applied to simulate temperatures, strains, and stresses during temperatures, which were expected during de-icing conditions of aircraft leading edges. The heater element temperature was (locally) increased from -25 to 86.7 °C within 4.8 s. This steeper temperature increase caused considerably higher compression stresses in the straight copper heater element. Furthermore, the magnitudes of the surface strain components above the heater element almost increased by the factor of four compared to the slow heating regime. This indicated larger deformation due to (local) bending of the structure. Hence, a compromise of allowable stresses and required heating rates needs to be found when using heated GLARE for de-icing of aircraft leading edges, as the aim of de-icing devices is to melt the accrued ice on the leading edges as fast as possible.

ACKNOWLEDGEMENTS

This study is partially funded by the Dutch Technology Foundation STW, Fokker Aerostructures, and by the H2020 project EXTREME, GA 636549.

ORCID

A. G. Anisimov  <http://orcid.org/0000-0002-0804-9103>

B. Müller  <http://orcid.org/0000-0002-2042-3217>

R. M. Groves  <http://orcid.org/0000-0001-9169-9256>

REFERENCES

- [1] M. Sinnett, *Boeing Aeromagazine* **2007**, 4, 6.
- [2] S. K. Thomas, R. P. Cassoni, C. D. MacArthur, *J. Aircr.* **1996**, 33, 841, <https://doi.org/10.2514/3.47027>.
- [3] C. Caliskan, C. Hajiyev, *Prog. Aerosp. Sci.* **2013**, 60, 12, <https://doi.org/10.1016/j.paerosci.2012.11.001>.
- [4] M. Mohseni, A. Amirfazli, *Cold Reg. Sci. Technol.* **2013**, 87, 47, <https://doi.org/10.1016/j.coldregions.2012.12.003>.
- [5] Fibre Metal Laminates Centre of Competence (FMLC), <http://www.fmlc.nl> (accessed: August 2017).
- [6] A. Vlot, J. W. Gunnink, *Fibre metal laminates—An introduction*, Kluwer Academic Publishers, Dordrecht, The Netherlands **2001**, doi: <https://doi.org/10.1007/978-94-010-0995-9>.
- [7] T. Sinmazcelik, E. Avcu, M. O. Bora, O. Coban, *Mater. Des.* **2011**, 32, 3671, <https://doi.org/10.1016/j.matdes.2011.03.011>.
- [8] R. C. Alderliesten, J. J. Homan, *Int. J. Fatigue* **2006**, 28(10), 1116, <https://doi.org/10.1016/j.ijfatigue.2006.02.015>.
- [9] C. Vermeeren, *Around GLARE—A new aircraft material in context*, Kluwer Academic Publishers, Dordrecht, The Netherlands **2002**, doi: <https://doi.org/10.1007/0-306-48385-8>.
- [10] A. Vlot, *GLARE—History of the development of a new aircraft material*, Kluwer Academic Publishers, Dordrecht, The Netherlands **2001**, doi: <https://doi.org/10.1007/0-306-48398-X>.
- [11] P. Krammer, D. Scholz, *Estimation of electrical power required for deicing systems*, Hamburg University of Applied Sciences, Germany **2009**.
- [12] Airplane and engine certification requirements in supercooled large drop, mixed phase, and ice crystal icing conditions, *Federal Register* 75 (124), Department of Transportation, Federal Aviation Administration (FAA) **2010**.
- [13] M. Hagenbeek, *PhD Thesis*, TU Delft **2005**.
- [14] P. Hofslagare, *J. Neutron Res.* **2003**, 11(4), 215, <https://doi.org/10.1080/10238160410001726639>.
- [15] M. Abouhamzeh, J. Sinke, R. Benedictus, *J. Compos. Mater.* **2015**, 49(14), 1705, <https://doi.org/10.1177/0021998314539776>.
- [16] B. Müller, S. Teixeira De Freitas, J. Sinke, Thermal cycling fiber metal laminates: Considerations, test setup and results. *Proc. of the ICCM: 20th Int. Conf. on Composite Materials* **2015**, 1.
- [17] B. Müller, S. Teixeira De Freitas, J. Sinke, Measuring thermal diffusion in fiber metal laminates. *Proc. of the ICAST: 25nd Int. Conf. on Adaptive Structures and Technologies* **2014**, 1.
- [18] B. Borgonje, M. S. Ypma, *Appl. Compos. Mater.* **2003**, 10, 243, <https://doi.org/10.1023/A:1025589812963>.
- [19] S. Y. Park, W. J. Choi, H. S. Choi, *Compos. Struct.* **2010**, 92(1), 18, <https://doi.org/10.1016/j.compstruct.2009.06.006>.
- [20] A. A. Costa, D. F. N. R. da Silva, D. N. Travessa, E. C. Botelho, *Mater. Des.* **2012**, 42(1), 434, <https://doi.org/10.1016/j.matdes.2012.06.038>.
- [21] V. M. Papadakis, B. Müller, M. Hagenbeek, J. Sinke, R. M. Groves, *Proc. SPIE* **2016**, 9804 98040S, doi: <https://doi.org/10.1117/12.2221919>.
- [22] B. Müller, M. Hagenbeek, J. Sinke, *Compos. Struct.* **2016**, 152, 106, <https://doi.org/10.1016/j.compstruct.2016.05.020>.
- [23] W. Steinchen, L. Yang, *Digital shearography: Theory and application of digital speckle pattern shearing interferometry*, SPIE Optical Engineering Press, Bellingham, Washington **2003**.
- [24] M. A. Sutton, J. J. Orteu, H. Schreier, *Image correlation for shape, motion and deformation measurements — Basic concepts, theory and applications*, Springer Science+Business Media **2009**, doi: <https://doi.org/10.1007/978-0-387-78747-3>.
- [25] Minimizing Noise and Bias in 3D DIC, www.correlatedsolutions.com/supportcontent/dic-noise-bias.pdf (accessed: August 2017).
- [26] P. Reu, *Exp. Tech.* **2014**, 38, <https://doi.org/10.1111/ext.12111>.
- [27] Y. Y. Hung, *Opt. Eng.* **1982**, 21, 213, <https://doi.org/10.1117/12.7972920>.
- [28] D. Francis, R. P. Tatam, R. M. Groves, *Meas. Sci. Technol.* **2010**, 21, 102, <https://doi.org/10.1088/0957-0233/21/10/102001>.
- [29] L. Yang, X. Xie, *Digital shearography: New developments and applications*, SPIE Optical Engineering Press, Bellingham, Washington **2016**, doi: <https://doi.org/10.1117/3.2235244>.
- [30] A. G. Anisimov, B. Müller, J. Sinke, R. M. Groves, *Proc. SPIE* **2015**, 9435, 943524, <https://doi.org/10.1117/12.2082636>.
- [31] B. Müller, A. G. Anisimov, J. Sinke, R. M. Groves, *Proc. of the ETNDT: Emerging Technologies in Non-Destructive Testing VI* **2015**, 6, 205.
- [32] A. G. Anisimov, R. M. Groves, *Proc. SPIE* **2015**, 9525, 952517, <https://doi.org/10.1117/12.2184058>.
- [33] S. W. James, R. P. Tatam, *Proc. SPIE* **1999**, 3744, 394, <https://doi.org/10.1117/12.357738>.
- [34] R. M. Groves, S. W. James, R. P. Tatam, *Proc. SPIE* **2003**, 4933, 135, <https://doi.org/10.1117/12.516623>.
- [35] J. Heikkilä, O. Silvén. A four-step camera calibration procedure with implicit image correction. *Proc. of IEEE Computer Society Conf. on Computer Vision and Pattern Recognition* **1997**, 1106.
- [36] J.Y. Bouget, R. Silva, L. Pardini, M. Rezende, Camera calibration toolbox for MATLAB **2004**.

- [37] A. G. Anisimov, M. G. Serikova, R. M. Groves, Development of the 3D shape shearography technique for strain inspection of curved objects. *Proc. of Imaging and Applied Optics* **2016**, DTh3C.4, doi:<https://doi.org/10.1364/DH.2016.DTh3C.4>.
- [38] K. J. A. Kundig, J. G. Cowie, in *Mechanical Engineers Handbook — Materials and mechanical design* (ed. M. Kutz), John Wiley & Sons, Inc., Hoboken, New Jersey **2006**, doi:<https://doi.org/10.1002/0471777447.ch4>.
- [39] M. Abouhamzeh, J. Sinke, R. Benedictus, *Compos. Struct.* **2015**, *122*, 546, <https://doi.org/10.1016/j.compstruct.2014.12.019>.
- [40] M. Pacchione, J. Telgkamp. Challenges of the metallic fuselage. *Proc. of the 25th Int. Congress of the Aeronautical Sciences (ICAS)* **2006**, *25*, 1.

How to cite this article: Anisimov AG, Müller B, Sinke J, Groves RM. Analysis of thermal strains and stresses in heated fibre metal laminates. *Strain*. 2018;54:e12260. <https://doi.org/10.1111/str.12260>